Chemical Science

ROYAL SOCIETY OF CHEMISTRY

EDGE ARTICLE

View Article Online
View Journal | View Issue

Cite this: *Chem. Sci.*, 2023, **14**, 9145

All publication charges for this article have been paid for by the Royal Society of Chemistry

Achieving desirable charge transport by porous frame engineering for superior 3D printed rechargeable Ni–Zn alkaline batteries†

Wenyu Cao, Haojie Li, Hui Ma, Jintao Fan and Xiaocong Tian *

Received 3rd June 2023
Accepted 2nd August 2023

DOI: 10.1039/d3sc02826g

rsc.li/chemical-science

Rechargeable 3D printed batteries with extraordinary electrochemical potential are typical contenders as one of the promising energy storage systems. Low-cost, high-safety, and excellent rechargeable aqueous alkaline batteries have drawn extensive interest. But their practical applications are severely hampered by poor charge carrier transfer and limited electrochemical activity at high loading. Herein, we report a unique structure-based engineering strategy in 3D porous frames using a feasible 3D printing technique and achieve 3D printed full battery devices with outstanding electrochemical performance. By offering a 3D porous network to provide prominently stereoscopic support and optimize the pore structure of electrodes, the overall charge carrier transport of engineered 3D printed Ni–Zn alkaline batteries (E3DP-NZABs) is greatly enhanced, which is directly demonstrated through a single-wired characterization platform. The obtained E3DP-NZABs deliver a high areal capacity of 0.34 mA h cm^{-2} at 1.2 mA cm^{-2}, and an outstanding capacity retention of 96.2% after 1500 cycles is also exhibited with an optimal electrode design. Particularly, parameter changes such as a decrease in pore sizes and an increase in 3D network thickness are favorable to resultant electrochemical performance. This work may represent a vital step to promote the practical application progress of alkaline batteries.

1. Introduction

One of the most dependable energy storage options for electric vehicles and modern electronics is rechargeable energy storage devices (RESDs).[1–4] Rechargeable aqueous zinc-based alkaline batteries are advanced RESDs due to their high safety, low cost, environmental friendliness, and high electrochemical potential.[5–7] Until now, a variety of aqueous zinc-based batteries such as Ni–Zn, Co–Zn, Ag–Zn and Zn–Air batteries have been widely reported.[8–11] Among them, rechargeable Ni–Zn alkaline batteries (NZABs) have drawn significant attention owing to their low cost and compelling electrochemical potentials.[12,13] The use of alkaline electrolytes can potentially reduce the costs of raw materials for preparation, solve the safety problem caused by flammable organic electrolytes, and avoid the excessive manufacturing to effectively reduce the consumption of energy and resources.[14,15] Meanwhile, due to the high redox potential value of Ni^{2+}/Ni^{3+} (0.59 V *vs.* Hg/HgO) and low redox potential of $Zn(OH)_4^{2-}/Zn$ (−1.26 V *vs.* SHE) in alkaline electrolytes, operating voltages reach 1.93 V, thus offering high-capacity ability.[16] However, compared with lithium-ion batteries, the rational three-dimensional (3D) construction of NZAB electrodes is rarely reported, leading to limited applications.

Structure design plays an important role in the improvement of the electrochemical performance of NZABs.[17,18] 3D NZAB structures with favorable porous architectures can significantly reduce the agglomeration of active materials during the charge–discharge process, while avoiding the formation of a discontinuous interface that may cause exfoliated and poor conductivity.[19–21] Previously reported architectures such as carbon cloth and carbon paper have been widely used for good conductivity and desirable mechanical strength although their resistance values are still higher than those of metals or alloys.[22,23] Additionally, uneven distribution of ion transport channels and low mass loading may still hinder the charge–discharge process with inconsistent ion distribution and sluggish diffusion kinetics at high current density, causing decaying electrochemical performance during cycling.[24–26] To this end, a well-designed 3D structure with better conductivity, good mechanical properties, a uniform pore structure, and distribution is eagerly needed towards desirable NZABs.

Compared with conventional methods, 3D printing that also referred to as additive manufacturing, has been regarded as an advanced manufacturing approach towards RESDs with customized geometries and controllable 3D structures.[27–29] Recently, based on 3D printing, a plenty of in-plane RESDs have been developed with remarkable electrochemical behaviors. Direct ink writing (DIW), representing a typical 3D printing technique, has great advantages in low cost and convenient manufacturing.[30,31] It has superiority in fabrication of RESDs with customized device geometries and complex configurations. Moreover, this technique

Faculty of Materials Science and Chemistry, China University of Geosciences, Wuhan 430074, China. E-mail: tianxc@cug.edu.cn

† Electronic supplementary information (ESI) available. See DOI: https://doi.org/10.1039/d3sc02826g

is highly capable of tuning the chemical components of printable ink and building high-performance RESDs.[32–34] 3D printing of RESDs could maintain the uniform distribution of materials on the surface of the 3D architecture, while homogenizing the cathode. By adjusting printing parameters, the load and distribution of active materials can be precisely controlled, thus improving NZAB performance. Unfortunately, it remains as a challenge in the NZAB field.

Herein, we develop a unique engineering strategy using 3D porous frames for superior 3D printed rechargeable NZABs with remarkable electrochemical behaviors. By engineering a wired acid-etched nickel foam (A-NF) as a 3D porous current collector frame to provide 3D network support for Ni-based cathodes by the DIW technique, electrical/ionic transport is significantly enhanced, which is directly confirmed from a single-wired characterization platform built by the 3D printing technique. With optimal manufacturing parameters, outstanding device areal capacities, high energy densities and good cycling stabilities are obtained for the engineered 3D printed NZABs (donated as E3DP-NZABs), demonstrating enhanced active sites and efficient structural optimization. Our methodology with 3D porous structure design ensures favorable microstructural metrics and desired electrochemical characteristics at a device level in comparison to conventional manufacturing approaches, signifying a significant advancement towards practical energy storage applications.

2. Results and discussion

The fabrication process of 3D printed NZABs mainly consisted of three major steps as shown in Fig. 1a. Prior to the DIW of Ni-based inks, the primary A-NF was prepared to interdigitated patterns that was compatible with the subsequent 3D printing programs (Fig. 1b). Electrodeposition was employed for desirable Zn-coating on the anode host, where a color change on the surface was observed (Fig. 1c and d), indicating a successful electrodeposition process. Notably, the surface states of NFs were important for the attachment of active materials. A-NF with surface treatment could not only facilitate the uniform deposition of zinc ions on surfaces, but also supply more active sites for electrochemical processes (Fig. S1†). In the following step, the interdigitated engineering NFs were fixed onto various substrates, for example quartz glass, for the DIW process.

The DIW process basically included ink loading in a syringe, ink extrusion from nozzles under pneumatic pressure, and ink deposition into a 3D porous current collector frame. To further address the poor electron transport issue of Ni-based active materials, super P was also added as a conductive additive. The 3D printing routine was predesigned and inputted into a 3D printer. Due to the superior capability of DIW technology in digitally controlling the patterns of deposited inks, even active material distribution has been realized. By precisely controlling the rheological properties of ink, the contact between the deposited ink and A-NF has been efficiently controlled, significantly affecting the performance of NZABs. Excessive materials would block the ion transport channels, reduce the area of active sites, and accelerate the unfavorable amassing of materials, ultimately worsening the battery performance. In contrast, less material loading might result in low space utilization as well as low device capacities.

Fig. 2a presents a photograph of E3DP-NZAB electrodes. The total area of the device was ~3.4 cm^2. As shown in Fig. S2,† the nanosheet morphology of NiCo-layered double hydroxides (NiCo-LDHs) was observed in scanning electron microscopy (SEM) images. In contrast to $Ni(OH)_2$, the synergistic effect from cobalt atom doping was favorable towards the generation of

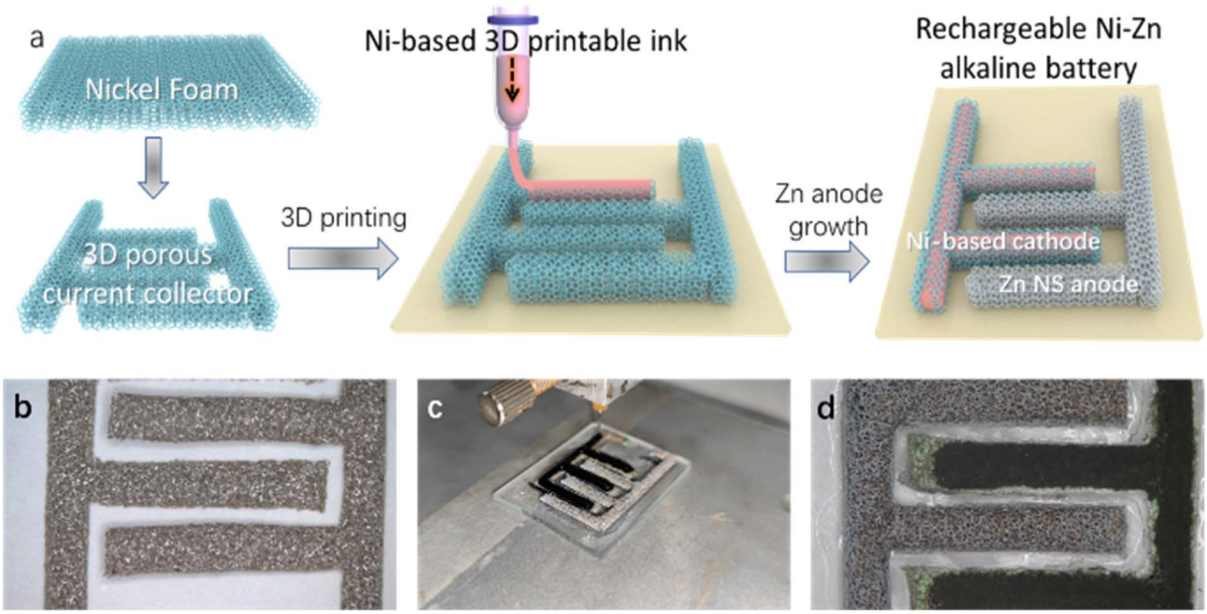

Fig. 1 (a) Schematic of the 3D printing-based fabrication process of NZABs with 3D porous frames. (b–d) Photographs showing the patterned A-NF current collector frame (b), a typical 3D printing process (c), and obtained NZAB electrodes (d).

more disordered structures, relieving the lattice change stress during electrochemical cycles and improving the electrochemical performance of E3DP-NZABs. A 3D conductive network and inner hierarchical structure inside the nickel-based cathode were further studied. As presented in Fig. 2b and S3a,† NiCo-LDH/C composites further combined with a 3D conductive framework to form a 3D cross-linked network significantly improve the space utilization inside the electrode and ensure the overall conductivity of the cathode. At higher magnifications, pores of tens of microns were clearly found for the Ni-based cathode (Fig. 2c, d and S3b†). It showed that the active materials were uniformly distributed with a reasonable hierarchical pore structure after the 3D printing process, which facilitated the infiltration of electrolyte ions into the electrode structure, improved the ion mobility, and ensured that 3D printed thick electrodes show highly expected electrochemical performance. More details showed that nickel-based active materials were tightly compounded with carbon materials, and nanosheet-like NiCo-LDHs were wrapped by carbon materials, which helped to address the limited conductivity issue of nickel-based active materials (Fig. 2e).

Additionally, EDS element mapping results for nickel-based cathodes verified homogeneous distribution of nickel, cobalt, carbon and oxygen elements (Fig. 2f). For the anode, as displayed in Fig. S4,† the Zn deposited A-NF anode can be indexed to Ni (JCPDS 04-0850) and Zn (JCPDS 04-0831); meanwhile obviously flower-like zinc deposits had been observed on the surface of the 3D conductive network (Fig. 2g and h), which is not only conducive to electron transport but also greatly reduces the negative impact of passive product accumulation and provides ample space for the temporary storage of zinc oxide produced during redox reactions. Meantime, the 3D structure of the zinc-based anode provides abundant reaction sites for redox reactions, while ensuring the integrity of the electrode structure because of not reacting with the electrolyte. The EDS images of the anode show that the distribution of zinc and nickel elements is uniform, proving that the Zn-based anode has excellent conductivity and relatively uniform electric field distribution (Fig. 2i and S5†).

The nickel-based cathodes were also studied through X-ray photoelectron spectroscopy (XPS).[35,36] In detail, the Ni 2p spectrum has four distinct main peaks (representing Ni $2p_{3/2}$ and Ni $2p_{1/2}$ peaks) and two satellite peaks (Fig. S6a and b†). With spin–orbit splitting, the main peaks could be attributed to Ni^{2+} (855.1 and 872.6 eV) and Ni^{3+} (856.4 and 874.1 eV). The peaks with a binding energy of 861.3 eV and 879.4 eV corresponded to the satellite peaks of Ni $2p_{3/2}$ and Ni $2p_{1/2}$ (marked as sat.), respectively. Similarly, the Co 2p spectrum shown in Fig. S6c† also presented four distinct main peaks (representing Co $2p_{3/2}$ and Co $2p_{1/2}$ peaks) and two satellite peaks. With spin–orbit splitting, the peaks at 797.6 and 781.8 eV corresponded to Co^{2+}, and the peaks at 780.7 and 796.2 eV were indexed to Co^{3+}. The

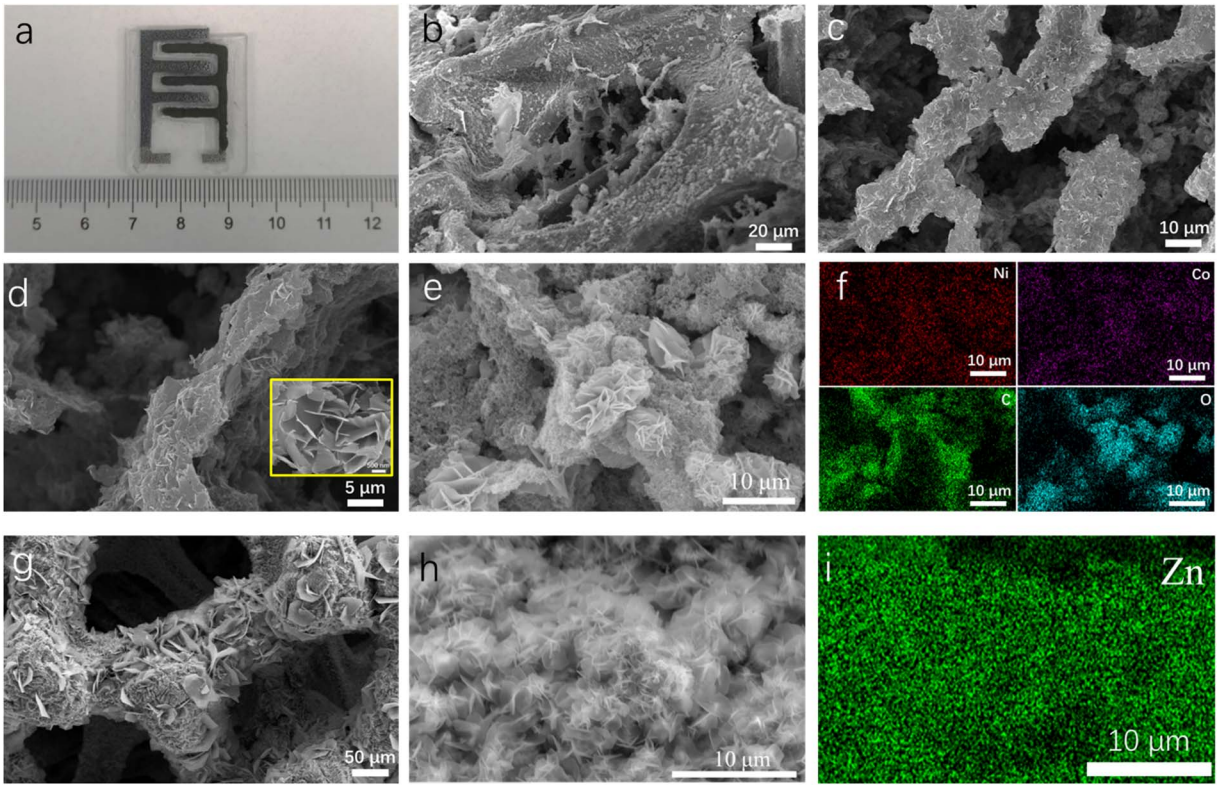

Fig. 2 (a) Photograph of E3DP-NZABs. (b–e) SEM images of E3DP-NZAB cathodes at various magnifications. (f) Corresponding EDS mapping images of Ni, Co, C, and O elements in (e). (g and h) SEM images of E3DP-NZAB anodes at different magnifications. (i) Corresponding EDS mapping images of Zn element for (h).

peaks with a binding energy of 786.4 and 802.9 eV corresponded to the satellite peaks of Co $2p_{3/2}$ and Co $2p_{1/2}$, respectively. The fitting results in the O 1s spectrum showed that the peak centered at 531.3 eV could be divided into three peaks (Fig. S6c†). The divided O1 (530.6 eV) represented the oxygen in the crystal structure, O2 (532.3 eV) belonged to oxygen vacancies, and O3 (531.3 eV) corresponded to the oxygen in the hydroxyl group. The peaks in the C 1s region were consistent with previous reports (Fig. S6d†).[37] This might indicate that NiCo-LDHs were well combined with carbon materials.[38]

To directly demonstrate the effectiveness of engineering optimization in electrode electrical transport, a single-wired electrode characterization platform was designed and constructed as schematically shown in Fig. 3a. This platform consists of a cathode wire, an anode wire, a space-confined electrolyte, and electrode contacts. By installing the platform onto the holder system obtained from a fused deposition modeling (FDM) 3D printer (Fig. 3b and S7†), the desirable measurement could thus be conducted. The single cathode wire used in the measurement contained single E3DP and unmodified 3D printed (U3DP) cathode wires. The measurement results are shown in Fig. 3c. At the initial state, the electrical resistance of the single E3DP cathode wire was much lower and remained at the same order of magnitude after cycles. In comparison, for the single U3DP cathode wire, the electrical resistances were much higher before and after cycles, directly indicating that the introduction of 3D structural frames could greatly enhance the overall electrical conductivity of the nickel-based electrodes, simultaneously facilitate ionic transport, and ultimately boost the electrochemical performance of NZABs.

NZABs with 3D structure frames demonstrated the enhancement of both electrical and ionic conductance for battery devices. These improved metrics were highly favorable to the overall electrochemical behaviors of NZABs (Fig. 3d). Although the electrode shapes of single E3DP and U3DP cathode wires were highly similar, the internal 3D structure greatly improved the electrical conductance since there were large differences in the charge carrier migration paths and numbers. On the one hand, the continuous channels of 3D structure frames greatly improved the electrical transport capacity, while the electrical conductance of the single U3DP cathode wire only relied on the conductivity of nickel-based cathode materials. On the other hand, compared with single U3DP cathode wires, 3D structure frames offered abundant pores, which provided rich active sites, improved the utilization rate of internal active materials, ensured sufficient contact between the electrolyte and electrodes, and built more channels for charge carrier transport, and therefore were expected to improve the electrochemical performance of E3DP batteries.

Further comparison of device electrochemical performance between U3DP-NZABs and E3DP-NZABs was conducted. In the measurement, the thickness and pore size of 3D structure frames were 2 mm and 110 pores per inch (PPI), respectively. Cyclic voltammetry (CV) curves (Fig. 4a) illustrated an enormous discrepancy for E3DP-NZABs and U3DP-NZABs. In detail, the difference in the intensity and position of the redox reaction-

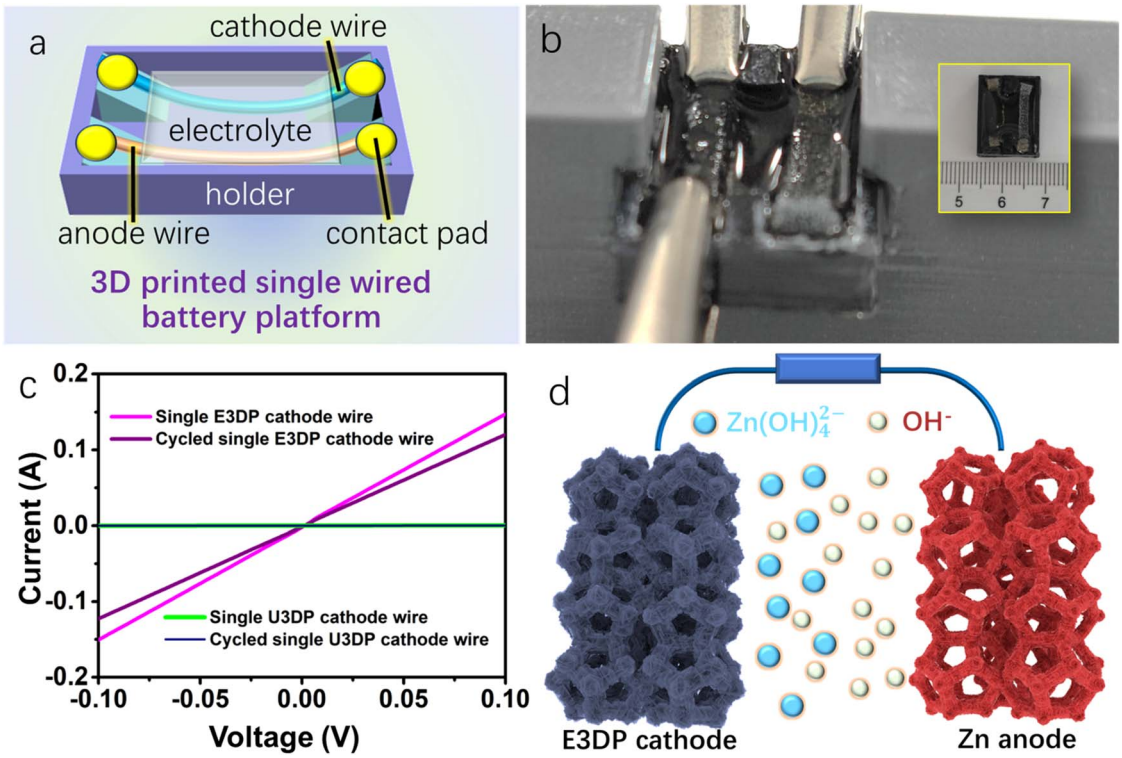

Fig. 3 (a) Schematic of 3D printed single-wired battery measurement devices. (b) Photograph of measurement platform devices. (c) *I*–*V* results of various 3D printed single cathode wires before and after electrochemical cycles. (d) Schematic of the charge storage mechanism of NZABs.

based peaks was revealed for the two differently structured NZABs, and the redox peaks of E3DP-NZABs were significantly stronger than those of U3DP-NZABs, which indicated more accessible active sites as well as the high reversibility of reactions for E3DP-NZABs. These peaks could be attributed to reactions that occurred on the electrodes. In the galvanostatic charge–discharge (GCD) test, E3DP-NZABs yielded the higher areal discharge capacity of 0.34 mA h cm^{-2} at a current density of 1.2 mA cm^{-2} (Fig. 4b), which was dozens of times that of U3DP-NZABs (0.01 mA h cm^{-2} at 1.2 mA cm^{-2}). In the meantime, a high voltage window of 1.9 V was operatable for E3DP-NZABs and a visible discharge plateau was exhibited, indicating enhanced electrochemical performance with the introduction of 3D structure frames. A lower voltage drop was also found for E3DP-NZABs, revealing lower internal resistance. Long-term cycling measurement further illustrated the influence of 3D structure frames on the electrochemical stability of batteries (Fig. 4c). During the charge–discharge process, E3DP-NZABs exhibited a preeminent capacity retention of 96.2% after 1500 cycles, while the capacity retention of U3DP-NZABs dropped to 16.6% under the same conditions. The results clearly demonstrated better stability and higher reactive reversibility of E3DP-NZABs, which might be attribute to inhibited structure degradation and reduced aggregation of active materials. Fig. 4d displays electrochemical impedance spectroscopy (EIS) results, where the charge transfer resistance (R_{ct}) of E3DP-NZABs was 4.4 Ω, lower than that of U3DP-NZABs (574.5 Ω). With the introduction of a 3D porous structure, E3DP-NZABs ensured the sufficient penetration of electrolyte ions throughout the electrode architectures, which thus largely shortened the ion-diffusion distance and promoted the utilization of the active sites.[39,40] The reduced ion diffusion resistance demonstrated the optimization effectiveness from a structure perspective for enhanced electrical and ionic conductivity of NZABs.

To access the desirable matching between the cathode and anode, E3DP-NZABs with different zinc deposition times were tested (Fig. S8†), where the size of 3D structure frames used in this test was fixed to 110 PPI (pore size) and 2 mm (thickness). With different zinc deposition times, the CV curves of various NZABs showed similar shapes (Fig. S8a†). When the zinc deposition time was 3600 s, the E3DP-NZABs displayed a maximum CV curve area, indicating that the zinc-based anode and cathode were optimally matched. This was also confirmed in galvanostatic discharge and rate performance results (Fig. S8b and c†). With a deposition time of 3600 s, the device exhibited the highest areal capacity of 0.34 mA h cm^{-2} at a current density of 1.2 mA cm^{-2}, while the areal capacities of devices with deposition periods of 1800, 5400, and 7200 s were 0.26, 0.29, and 0.24 mA h cm^{-2}, respectively. The rate capacity and coulombic efficiency results also demonstrated that devices with a zinc deposition time of 3600 s possessed an optimal electrochemical performance (Fig. S8d and e†). The R_{ct} values of devices with zinc deposition times of 1800, 3600, 5400, and 7200 s were 6.99, 4.38, 8.82, and 8.03 Ω, respectively, which also confirmed the key effects of zinc deposition time on not only

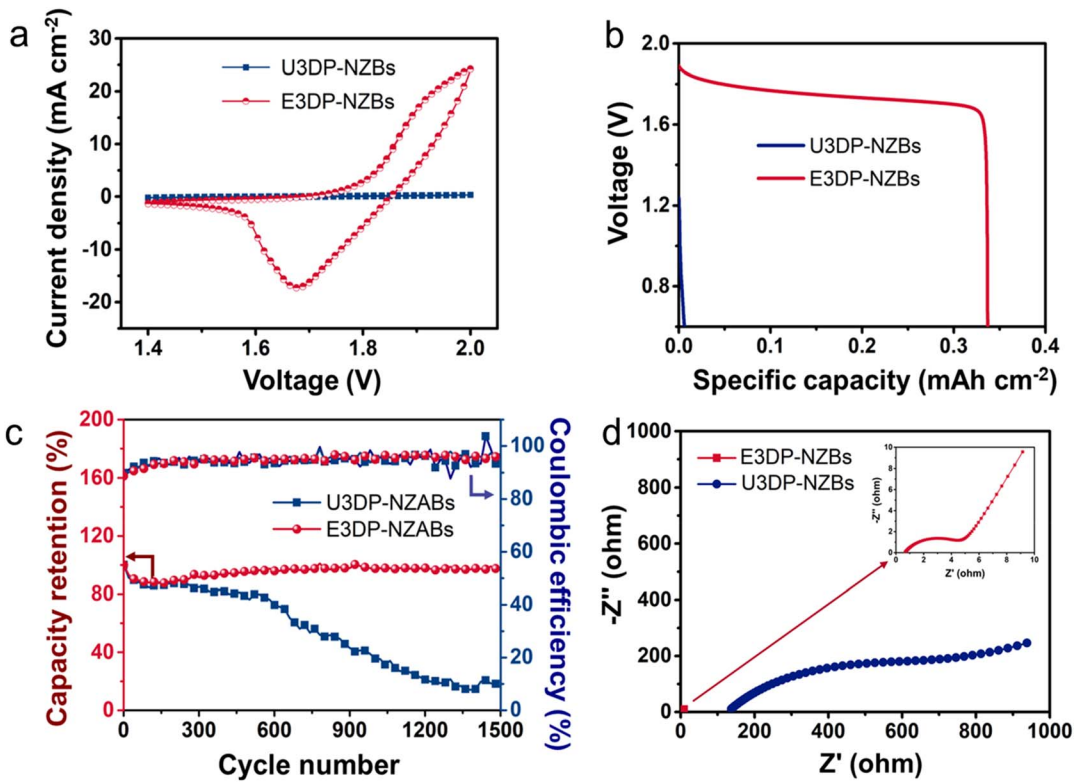

Fig. 4 Comparison between U3DP-NZABs and E3DP-NZABs. (a) CV curves at a scan rate of 10 mV s^{-1}. (b) Galvanostatic discharge curves at a current density of 1.2 mA cm^{-2}. (c) Long-term cycling performance. (d) EIS curves.

electrochemical performance, but also charge carrier transport characteristics (Fig. S8f†). Detailed electrochemical measurement results of devices with different zinc deposition times of 1800, 5400, and 7200 s are exhibited in Fig. S9.†

To evaluate the effect of 3D frame sizes on battery electrochemical performance, E3DP-NZABs with 3D structure frames of different pore sizes and thicknesses were fabricated and compared. With the same thickness (2 mm), E3DP-NZABs with different pore sizes of 3D structures were first tested in terms of device electrochemical behaviors. As shown in Fig. 5a, E3DP-NZABs with a pore size of 110 PPI exhibited the largest CV curve area, indicating abundant redox sites and an optimal pore size parameter among the tested samples. The highest device capacities were calculated to be 0.34 mA h cm^{-2} at a current density of 1.2 mA cm^{-2} for E3DP-NZABs with 110 PPI (Fig. 5b), while the capacities of the other two types of E3DP-NZABs with pore sizes of 75 and 35 PPI were 0.21 and 0.12 mA h cm^{-2}, respectively. This indicated that the capacity of E3DP-NZABs gradually increased as the pore size of 3D structure frames decreased. This might be attribute to more active sites as well as enhanced charge carrier transport with 110 PPI. In this regard, with 3D porous frames of over 110 PPI, higher electrochemical performance of E3DP-NZABs is higher expected to exceed the obtained values based on the basic design principle on charge carrier transport in this work. Nevertheless, the accompanying side reactions caused by higher utilization of active materials should also be noted, due to which the cycling stability might be significantly affected. Within the unit volume, the capacities of the three different E3DP-NZABs maintained a nearly identical trend with the change of current density values (Fig. 5c and S10a†), indicating that the device electrochemical behaviors of E3DP-NZABs were closely related to the structural design.

Further analysis was conducted on the electrochemical performance evolution of E3DP-NZABs with the same pore size (110 PPI) but different thicknesses of 3D structure frames. As shown in Fig. S10b,† E3DP-NZABs with the 2 mm thickness possessed the largest CV curve area. As the thickness decreased, the CV curve area decreased as well. This was also confirmed by galvanostatic discharge curves (Fig. S10c†), where the highest capacity was achieved for 2 mm-thick electrodes at a current density of 1.2 mA cm^{-2}. Device capacities with other thicknesses decreased to 0.29, 0.22, and 0.20 mA h cm^{-2} (Fig. 5d and

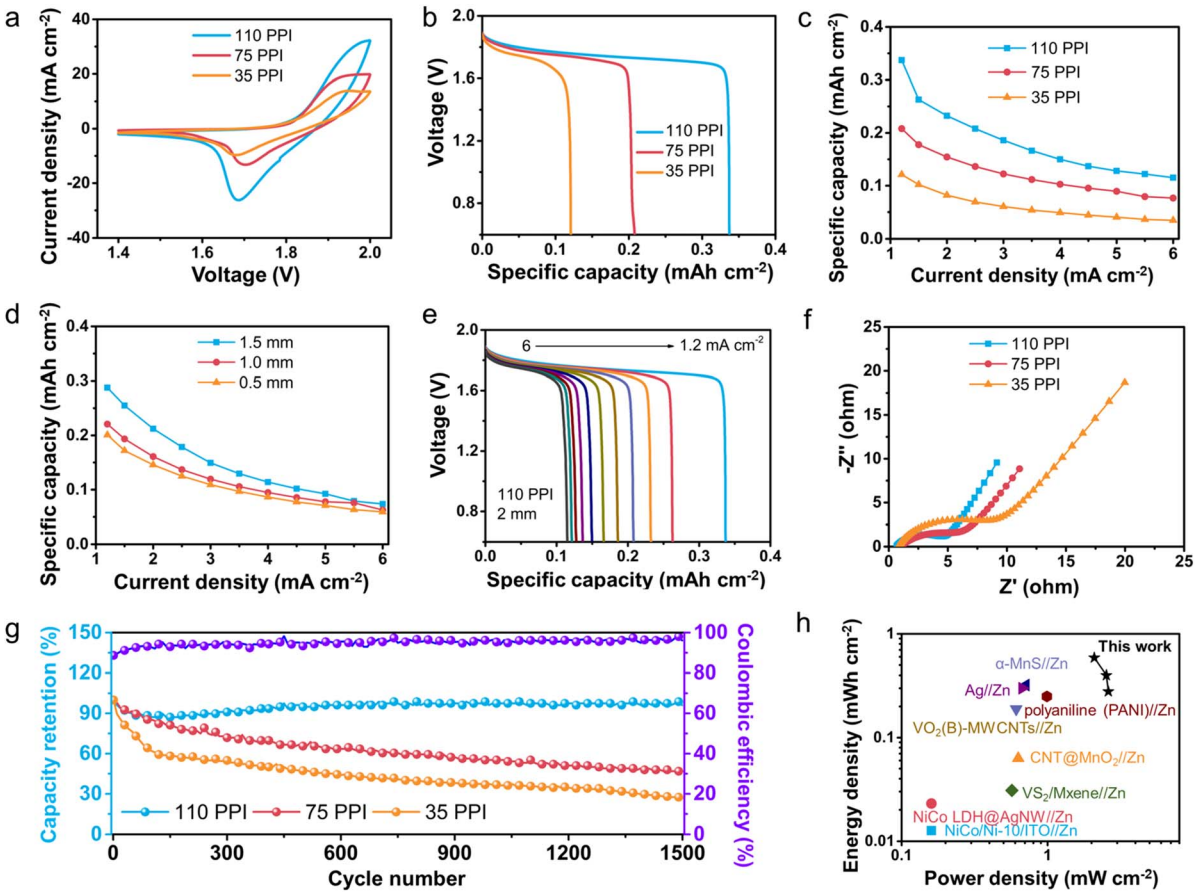

Fig. 5 Comparison of various E3DP-NZBs with different 3D structure frames. (a) CV curves at a scan rate of 10 mV s^{-1}. (b) Galvanostatic discharge curves at a current density of 1.2 mA cm^{-2}. (c) Device areal capacity profiles at various current densities. (d) Device areal capacity profiles of E3DP-NZBs with different thicknesses. (e) Galvanostatic discharge curves of E3DP-NZBs with a 110 PPI (pore size) and 2 mm (thickness) 3D structure. (f) EIS curves of E3DP-NZBs with different pore-sized 3D structures. (g) Long-cycling stability of E3DP-NZABs with different pore-sized 3D structures. (h) Ragone plots showing the energy and power densities of E3DP-NZBs as compared with those of previously reported devices.

S10d†). It clearly demonstrated that thicker batteries exhibit superior capacities at the same current density, and directly confirmed the efficiency of 3D structural design for 3D printed NZABs.

Experimental measurements have proven that E3DP-NZABs with pores sized 110 PPI and a thickness of 2 mm exhibited the best electrochemical performance. Their CV and galvanostatic discharge profiles are further displayed in Fig. S10e.† The obvious redox peaks were observed, and similar shapes at different scan rates were found, revealing good reactive reversibility and electrochemical stability of E3DP-NZABs. Fig. 5e shows that the battery delivered a moderate voltage window and a stable discharge platform. At a current density of 6 mA cm^{-2}, the capacities could still reach 0.11 mA h cm^{-2}. The Nyquist plots (Fig. 5f and S10f†) confirmed the successful establishment of ideal ion/electron transport channels and excellent electrochemical performance of E3DP-NZABs with optimal size parameters.

The long-term cycling stability of E3DP-NZABs was also evaluated. After 1500 cycles, the capacity retention of E3DP-NZABs with a pore size of 110 PPI and a thickness of 2 mm remained at 96.2%. The SEM images of electrodes after cycling were further collected and displayed in Fig. S11,† where the morphologies of both cycled cathodes and anodes were still maintained well, directly illustrating the high electrochemical stability of E3DP-NZBs. As the pore size of E3DP-NZABs increased to 75 PPI and 35 PPI, the capacity retentions were 46.9% and 26.9%, respectively, after 1500 cycles (Fig. 5g). Meanwhile, as the thickness of 3D structure frames decreased to 1.5, 1, and 0.5 mm, the capacity retention values of E3DP-NZABs decreased to 39.8%, 28.6%, and 35.8%, respectively, along with lower coulombic efficiencies (Fig. S10g and h†). Notably, for E3DP-NZBs with 110 PPI, a slight capacity increase during the charge–discharge process was found, which might be because a few deep active sites in E3DP cathodes were gradually activated with sufficient electrolyte–electrode contact and efficient charge carrier transport. In comparison, almost all active sites were directly utilized for E3DP-NZBs with 35 PPI and 75 PPI. These results clearly illustrated that the obtained E3DP-NZABs with optimal structures also exhibited high electrochemical reversibility during long-term cycles. It is noteworthy that the device areal energy and power density values of E3DP-NZABs reached 588 μW h cm^{-2} and 2.09 mW cm^{-2}, respectively, which surpassed some of the reported planar batteries (Fig. 5h).[41–48] Moreover, using the same engineering approach, E3DP-NZAB electrodes with various geometries could be readily achieved with good discharge behaviors (Fig. S12†). It further supported the superiority of our manufacturing approach as compared with previously reported conventional methods.[49–51] The detailed electrochemical performance of E3DP-NZABs with other pore sizes and thicknesses is shown in Fig. S13 and S14.†

3. Conclusion

In this work, we adopted a structural engineering strategy to optimize aqueous NAZBs with the help of a DIW-based 3D printing technique. By introducing 3D porous A-NFs as current collector frames to provide preeminent stereoscopic support for Ni-based cathodes, aqueous E3DP-NAZBs were constructed. Compared with 3D printed NAZBs without 3D structure frames, the charge carrier transport of electrodes in E3DP-NAZBs was greatly enhanced from a single-wired characterization platform. Electrochemical test results showed that the as-obtained E3DP-NAZBs exhibited a high areal capacity of 0.34 mA h cm^{-2}, which exceeded those of many previously reported batteries and capacitors. Meanwhile, long-term cycling stability was realized as well for E3DP-NAZBs, demonstrating the advantage of E3DP structures. Furthermore, with changes in the pore size and thickness of 3D structure frames, the influence of these parameters on the electrochemical performance of E3DP-NAZBs was studied, and the results showed that with an increased pore size or decreased thickness of 3D structure frames in the electrodes, device capacities decreased, reflecting the desirable charge transport by porous frame engineering for superior 3D printed rechargeable Ni–Zn alkaline batteries. These advantages and findings reveal that unique electrode manufacturing along with structural engineering can efficiently improve the electrochemical performance and practicality of batteries with great prospects.

Data availability

Data are available on request to the authors.

Author contributions

W. Cao: conceptualization, investigation, formal analysis, data curation, writing – original draft and writing – review & editing. H. Li, H. Ma and J. Fan: investigation, formal analysis and writing – review & editing. X. Tian: conceptualization, supervision, funding acquisition, project administration and writing – review & editing.

Conflicts of interest

None of the other authors have potential conflict of financial interest in this paper.

Notes and references

1 Y. Liu, X. Lu, F. Lai, T. Liu, P. R. Shearing, I. P. Parkin, G. He and D. J. L. Brett, Rechargeable aqueous Zn-based energy storage devices, *Joule*, 2021, **5**, 2845–2903.
2 Q. Huang, J. Wang, H. Gong, Q. Zhang, M. Wang, W. Wang, J. P. Nshimiyimana and X. Diao, A rechargeable electrochromic energy storage device enabling effective energy recovery, *J. Mater. Chem. A*, 2021, **9**, 6451–6459.
3 X. Wang, S. Zheng, F. Zhou, J. Qin, X. Shi, S. Wang, C. Sun, X. Bao and Z.-S. Wu, Scalable fabrication of printed Zn//MnO_2 planar micro-batteries with high volumetric energy density and exceptional safety, *Natl. Sci. Rev.*, 2020, **7**, 64–72.
4 X. Wang, J. Qin, Q. Hu, P. Das, P. Wen, S. Zheng, F. Zhou, L. Feng and Z.-S. Wu, Multifunctional mesoporous polyaniline/graphene nanosheets for flexible planar

integrated microsystem of zinc ion microbattery and, *Gas Sens.*, 2022, **18**, 2200678.

5 Q. Zhang, X. Liu, X. Zhu, Y. Wan and C. Zhong, Interface engineering of zinc electrode for rechargeable alkaline zinc-based batteries, *Small Methods*, 2023, **7**, e2201277.

6 R. Jayakumar, D. M. Harrison, J. Xu, A. V. Suresh Babu, C. Luo and L. Ma, Interphases in aqueous rechargeable zinc metal batteries, *J. Mater. Chem. A*, 2023, **11**, 8470–8496.

7 S. Lei, Z. Liu, C. Liu, J. Li, B. Lu, S. Liang and J. Zhou, Opportunities for biocompatible and safe zinc-based batteries, *Energy Environ. Sci.*, 2022, **15**, 4911–4927.

8 S. Chen, C. Peng, D. Xue, L. Ma and C. Zhi, Alkaline tolerant antifreezing additive enabling aqueous Zn||Ni battery operating at -60 degrees C, *Angew. Chem., Int. Ed. Engl.*, 2022, **61**, e202212767.

9 K. Sun, Y. Shen, J. Min, J. Pang, Y. Zheng, T. Gu, G. Wang and L. Chen, MOF-derived Zn/Co co-doped MnO/C microspheres as cathode and Ti3C_2@Zn as anode for aqueous zinc-ion full battery, *Chem. Eng. J.*, 2023, **454**, 140394.

10 G. Liang, F. Mo, D. Wang, X. Li, Z. Huang, H. Li and C. Zhi, Commencing mild Ag–Zn batteries with long-term stability and ultra-flat voltage platform, *Energy Storage Mater.*, 2020, **25**, 86–92.

11 P. Qi, M. Chen, T. Luo, C. Zhao, C. Lin, H. Luo and D. Zhang, Solid-state self-catalyzed growth of N-doped carbon tentacles on an M(Fe, Co)Se surface for rechargeable Zn–air batteries, *Chem. Commun.*, 2023, **59**, 5898–5901.

12 K. Zhou, S. Wang, G. Zhong, J. Chen, Y. Bao and L. Niu, Hierarchical heterostructure engineering of layered double hydroxides on nickel sulfides heteronanowire arrays as efficient cathode for alkaline aqueous zinc batteries, *Small*, 2022, **18**, e2202799.

13 L. Li, S. Cheng, L. Deng, T. Liu, W. Dong, Y. Liu, L. Huang, H. Yao and X. Ji, Effective solution toward the issues of Zn-based anodes for advanced alkaline Ni-Zn batteries, *ACS Appl. Mater. Interfaces*, 2023, **15**, 3953–3960.

14 Z. Cai, J. Wang and Y. Sun, Anode corrosion in aqueous Zn metal batteries, *eScience*, 2023, **3**, 100093.

15 S. Wu, Z. Hu, P. He, L. Ren, J. Huang and J. Luo, Crystallographic engineering of Zn anodes for aqueous batteries, *eScience*, 2023, **3**, 100120.

16 L. Li, Q. Cao, Y. Wu, Y. Zheng, H. Tang, J. Ge, M. Liang, B. Zhou, B. Jiang, S. Wu, F. Wang, Y. Pang, Z. Shen, C. Guan and H. Chen, Wood-derived continuously oriented three-phase interfacial channels for high-performance quasi-solid-state alkaline zinc batteries, *Adv. Mater.*, 2023, e2300132.

17 P. Man, B. He, Q. Zhang, Z. Zhou, C. Li, Q. Li, L. Wei and Y. Yao, A one-dimensional channel self-standing MOF cathode for ultrahigh-energy-density flexible Ni–Zn batteries, *J. Mater. Chem. A*, 2019, **7**, 27217–27224.

18 J. Yao, H. Wan, C. Chen, J. Ji, N. Wang, Z. Zheng, J. Duan, X. Wang, G. Ma, L. Tao, H. Wang, J. Zhang and H. Wang, Oxygen-defect enhanced anion adsorption energy toward super-rate and durable cathode for Ni-Zn batteries, *Nano-Micro Lett.*, 2021, **13**, 167.

19 J. W. Long, B. Dunn, D. R. Rolison and H. S. White, 3D architectures for batteries and electrodes, *Adv. Energy Mater.*, 2020, **10**, 2002457.

20 N. Guo, W. Huo, X. Dong, Z. Sun, Y. Lu, X. Wu, L. Dai, L. Wang, H. Lin, H. Liu, H. Liang, Z. He and Q. Zhang, A review on 3D zinc anodes for zinc ion batteries, *Small Methods*, 2022, **6**, e2200597.

21 W. Yang, L. Xu, W. Luo, M. Li, P. Hu, Y. Dai, F. Ye, C. Han, M. Zhou, R. Tu, J. Shi and L. Mai, 3D macroporous frame based microbattery with ultrahigh capacity, energy density, and integrability, *Adv. Energy Mater.*, 2023, **13**, 2300574.

22 J. Gong, W. Luo, Y. Zhao, M. Xie, J. Wang, J. Yang and Y. Dai, Co_9S_8/$NiCo_2S_4$ core-shell array structure cathode hybridized with PPy/MnO_2 core-shell structure anode for high-performance flexible quasi-solid-state alkaline aqueous batteries, *Chem. Eng. J.*, 2022, **434**, 134640.

23 Z. Li, Z. Deng, L. Ouyang, X. Fan, L. Zhang, S. Sun, Q. Liu, A. A. Alshehri, Y. Luo, Q. Kong and X. Sun, CeO_2 nanoparticles with oxygen vacancies decorated N-doped carbon nanorods: A highly efficient catalyst for nitrate electroreduction to ammonia, *Nano Res.*, 2022, **15**, 8914–8921.

24 X. Xia, J. Yang, Y. Liu, J. Zhang, J. Shang, B. Liu, S. Li and W. Li, Material choice and structure design of flexible battery electrode, *Adv. Sci.*, 2023, **10**, e2204875.

25 Y. Li and S. Guo, Material design and structure optimization for rechargeable lithium-sulfur batteries, *Matter*, 2021, **4**, 1142–1188.

26 J. Pu, Z. Liu, Z. Ma, J. Wang, L. Zhang, S. Chang, W. Wu, Z. Shen and H. Zhang, Structure design of $NiCo_2O_4$ electrodes for high performance pseudocapacitors and lithium-ion batteries, *J. Mater. Chem. A*, 2016, **4**, 17394–17402.

27 D. Yen, C.-H. Lin, D. J. Sprouster, X. Zheng, X. Xiao, W.-K. Lee, M. Ge and Y.-c. K. Chen-Wiegart, Nanotomography investigation of 3D printed batteries with a water-in-salt gel polymer electrolyte, *ACS Mater. Lett.*, 2023, 1466–1475.

28 S. Zhou, I. Usman, Y. Wang and A. Pan, 3D printing for rechargeable lithium metal batteries, *Energy Storage Mater.*, 2021, **38**, 141–156.

29 C. Liu, Y. Lao, F. Yang, X. Gong, X. Wang, L. Jiang, Z. Zeng and D. Yu, High-performance fiber-shaped Li-ion battery enabled by a surface-reinforced self-supporting electrode, *Chem. Commun.*, 2023, **59**, 6064–6067.

30 C. Zhu, N. B. Schorr, Z. Qi, B. R. Wygant, D. E. Turney, G. G. Yadav, M. A. Worsley, E. B. Duoss, S. Banerjee, E. D. Spoerke, A. van Buuren and T. N. Lambert, Direct ink writing of 3D Zn structures as high-capacity anodes for rechargeable alkaline batteries, *Small Struct.*, 2022, **4**, 2200323.

31 J. Bae, S. Oh, B. Lee, C. H. Lee, J. Chung, J. Kim, S. Jo, S. Seo, J. Lim and S. Chung, High-performance, printable quasi-solid-state electrolytes toward all 3D direct ink writing of shape-versatile Li-ion batteries, *Energy Storage Mater.*, 2023, **57**, 277–288.

32 G. Costa, P. A. Lopes, A. L. Sanati, A. F. Silva, M. C. Freitas, A. T. de Almeida and M. Tavakoli, 3D printed stretchable liquid gallium battery, *Adv. Funct. Mater.*, 2022, **32**, 2113232.
33 W. Gao and M. Pumera, 3D printed nanocarbon frameworks for Li-Ion battery cathodes, *Adv. Funct. Mater.*, 2021, **31**, 2007285.
34 S. Duraivel, D. Laurent, D. A. Rajon, G. M. Scheutz, A. M. Shetty, B. S. Sumerlin, S. A. Banks, F. J. Bova and T. E. Angelini, A silicone-based support material eliminates interfacial instabilities in 3D silicone printing, *Science*, 2023, **379**, 1248–1252.
35 H. N. Dhandapani, D. Mahendiran, A. Karmakar, P. Devi, S. Nagappan, R. Madhu, K. Bera, P. Murugan, B. R. Babu and S. Kundu, Boosting of overall water splitting activity by regulating the electron distribution over the active sites of Ce doped NiCo–LDH and atomic level understanding of the catalyst by DFT study, *J. Mater. Chem. A*, 2022, **10**, 17488–17500.
36 J. Li, L. Wang, H. He, Y. Chen, Z. Gao, N. Ma, B. Wang, L. Zheng, R. Li, Y. Wei, J. Xu, Y. Xu, B. Cheng, Z. Yin and D. Ma, Interface construction of NiCo LDH/NiCoS based on the 2D ultrathin nanosheet towards oxygen evolution reaction, *Nano Res.*, 2022, **15**, 4986–4995.
37 F. Wu, G. T. Kim, T. Diemant, M. Kuenzel, A. R. Schür, X. Gao, B. Qin, D. Alwast, Z. Jusys, R. J. Behm, D. Geiger, U. Kaiser and S. Passerini, Reducing capacity and voltage decay of Co-free $Li_{1.2}Ni_{0.2}Mn_{0.6}O_2$ as positive electrode material for lithium batteries employing an ionic liquid-based electrolyte, *Adv. Energy Mater.*, 2020, **10**, 2001830.
38 S. Lee, W. Li, A. Dolocan, H. Celio, H. Park, J. H. Warner and A. Manthiram, In-depth analysis of the degradation mechanisms of high-nickel, low/No-cobalt layered oxide cathodes for lithium-ion batteries, *Adv. Energy Mater.*, 2021, **11**, 2100858.
39 B. Yao, H. Peng, H. Zhang, J. Kang, C. Zhu, G. Delgado, D. Byrne, S. Faulkner, M. Freyman, X. Lu, M. A. Worsley, J. Q. Lu and Y. Li, Printing porous carbon aerogels for Low temperature supercapacitors, *Nano Lett.*, 2021, **21**, 3731–3737.
40 M. Liu, B. Li, H. Zhou, C. Chen, Y. Liu and T. Liu, Extraordinary rate capability achieved by a 3D "skeleton/skin" carbon aerogel–polyaniline hybrid with vertically aligned pores, *Chem. Commun.*, 2017, **53**, 2810–2813.
41 X. Xuan, M. Qian, L. Pan, T. Lu, Y. Gao, Y. Niu and S. Gong, A NiCo bimetallic hydroxide electrode-based flexible Ni//Zn battery with smart electrochromic function for visually monitoring battery residual electricity, *Sci. China Mater.*, 2022, **66**, 567–576.
42 X. Xuan, M. Qian, L. Pan, T. Lu, Y. Gao, L. Han, L. Wan, Y. Niu and S. Gong, A hollow tubular NiCo layacknered double hydroxide@Ag nanowire structure for high-power-density flexible aqueous Ni//Zn battery, *J. Energy Chem.*, 2022, **70**, 593–603.
43 Y. Ren, F. Meng, S. Zhang, B. Ping, H. Li, B. Yin and T. Ma, CNT@MnO_2 composite ink toward a flexible 3D printed micro-zinc-ion battery, *Carbon Energy*, 2022, **4**, 446–457.
44 J. Shi, S. Wang, X. Chen, Z. Chen, X. Du, T. Ni, Q. Wang, L. Ruan, W. Zeng and Z. Huang, An ultrahigh energy density quasi-solid-State zinc ion microbattery with excellent flexibility and thermostability, *Adv. Energy Mater.*, 2019, **9**, 1901957.
45 Y. Feng, Y. Feng, Y. Zhang, L. Sun, X. Li, M. Meng, Y. Zhu and K. Liu, Flexible zinc-ion microbattery based on a VS_2/MXene cathode with high cycle life, *J. Power Sources*, 2022, **545**, 231944.
46 K. Jiang, Z. Zhou, X. Wen and Q. Weng, Fabrications of high-performance planar zinc-ion microbatteries by engraved soft templates, *Small*, 2021, **17**, e2007389.
47 S. Bi, F. Wan, S. Wang, S. Jia, J. Tian and Z. Niu, Flexible and tailorable quasi-solid-state rechargeable Ag/Zn microbatteries with high performance, *Carbon Energy*, 2020, **3**, 167–175.
48 R. Li, L. Li, R. Jia, K. Jiang, G. Shen and D. Chen, A flexible concentric circle structured zinc-ion micro-battery with electrodeposited electrodes, *Small Methods*, 2020, **4**, 2000363.
49 Z. Wang, P. Shi, Q. Liu, J. Li, Y. Gan, J. Yao, J. Xia, X. Liu, X. Chen, K. Qian, X. Liu, L. Lv, G. Ma, L. Tao, J. Zhang, H. Wang, H. Wan and H. Wang, Enhanced polymerization interface of Ni12P5 nanowires toward high-rate and durable cathode for alkaline Ni–Zn batteries, *J. Power Sources*, 2022, **550**, 232170.
50 D. Liu, W. Xu, D. Zheng, Y. Wang, F. Wang, L. Zhou, Z. Nie and X. Lu, Sulfur doped $NiCo_2O_4$ nanosheets as advanced cathode for flexible alkaline Zn batteries, *J. Power Sources*, 2023, **571**, 233088.
51 L. Zhou, Q. Liu, X. Ma, P. Sun, X. Lv, L. Fang, X. Sun and M.-H. Shang, High areal energy density and super durable aqueous rechargeable NiCo//Zn battery with hierarchical structural cobalt–nickel phosphate octahydrate as binder-free cathode, *Chem. Eng. J.*, 2022, **450**, 138035.